Seismic Microwave Brightness Temperature Anomaly Detection Using Multitemporal Passive Microwave Satellite Images: Ideas and Limits

Yuan Qi , *Graduate Student Member, IEEE*, Zelang Miao , *Member, IEEE*, Lixin Wu, and Yifan Ding

Abstract—Thermal anomalies related to large earthquakes are frequently reported, but focus on the inconsistencies and uncertainties in the uncovered results caused by the diverse method used, data used, and case studies is lacking. Taking seismic anomaly detection using passive microwave remote sensing as an example, this study revealed and illustrated the time series of microwave brightness temperature (MBT) anomaly associated with the May 2008 Wenchuan earthquake, the April 2010 Yushu earthquake, the April 2013 Lushan earthquake, and the April and May 2015 Nepal earthquake sequence. Cross comparison showed that the spatial distribution of MBT anomalies behaves differently with different background-removal methods. More regional and detailed MBT anomalies (but with weaker intensities) were obtained with higher frequency data, whereas more pronounced MBT anomalies (but with fewer details) were acquired with lower frequency data. The amplitude and spatial scales of MBT anomalies at H polarization were larger than that at V polarization. And 10.7 GHz at H polarization was recommended as the optimal band. The spatiotemporal evolutions of MBT anomalies associated with the four selected earthquake cases were compared and found to be closely related to respective earthquake preparation mechanisms. The aforementioned characteristics and uncertainties of MBT anomalies under different conditions were then discriminated and discussed based on microwave remote-sensing physics, and the applications and limitations of the present study were illustrated and analyzed. The findings of this study are of great significance for remote sensing data selection, reliability assessment, and result interpretation in seismic-anomaly research.

Index Terms—Microwave brightness temperature (MBT), multitemporal image, seismic anomaly, time-series analysis, uncertainty.

I. INTRODUCTION

SINCE the 1980s, satellite infrared radiative data have been applied to detect multitemporal thermal anomaly prior to some medium-to-strong earthquakes [1]–[13]. Using mid-infrared band and thermal infrared band for seismic-anomaly monitoring are considered as a promising method by numerous remote-sensing and seismology researchers [1], [2], [5], [13]. With the launch of several passive microwave remote-sensing satellites in recent years, microwave brightness temperature (MBT) images are adopted to retrieve seismic anomaly for its consecutiveness and effectiveness [14]–[23]. MBT data can reflect the thermal radiation of the earth's surface at a certain depth owing to its ability to penetrate the atmosphere and ground surface [24]. Passive microwave satellite instruments are commonly equipped with multiple frequency channels (ranging from a few gigahertz to a few dozen) at dual-polarization modes (Horizontal polarization and Vertical polarization, H & V in brief), thereby providing various options for observing earth's surface radiative information.

Maeda and Takano [15], [16] proposed an anomaly index algorithm based on temperature difference between adjacent pixels to monitor seismic anomaly associated with the February 2004 Morocco earthquake and the May 2008 Wenchuan earthquake using MBT data with 18.7 GHz from the Advanced Microwave Scanning Radiometer for EOS (AMSR-E) instrument, and found that significant anomalies occurred near the mainshock epicenters. Referring to the overall trend of temperature change, Yang and Guo [21] observed the abnormal MBT prior to the April 2010 Baja California earthquake using AMSR-E data with 89 GHz. Singh *et al.* [18] reported both ascending and descending MBT anomalies associated with the May 2008 Wenchuan earthquake using satellite data with 19 and 37 GHz from the Special Sensor Microwave/Imager (SSM/I). Furthermore, Jing *et al.* [19] analyzed thermal anomalies associated with two earthquakes that occurred at the Tibetan Plateau by using segmented threshold method with SSM/I MBT data; it was found that MBT at 19 GHz was more sensitive to seismic anomalies than other higher frequencies. These case studies confirm that multitemporal MBT data with multiple frequencies can retrieve seismic anomaly. However, owing to the different research methods used, the results for different frequencies and for different cases are not comparable; thus, the spatiotemporal pattern of seismic anomaly under different conditions and the reasons for discrepant results require further consideration.

By using SSM/I data with 19 and 37 GHz at H and V polarization modes, Singh *et al.* [18] observed a bell-shaped MBT rise prior to the main shock of the May 12, 2008 Wenchuan earthquake. The result showed that the absolute values of the MBT with 19 and 37 GHz at V polarization are higher than that at H polarization. However, the maximum increments of

MBT at H polarization are about 10 K for 19 GHz and 15 K for 37 GHz, which is higher than that at V polarization for both bands. This finding reveals an easily overlooked phenomenon that satellite-observed MBT and the perturbation increment in seismic MBT anomaly behave inconsistently with different polarizations, which also indicates uncertainty in the results of seismic thermal anomalies.

Jing *et al.* [23] reported MBT anomalies associated with three strong earthquakes in Sichuan province, China, including the May 2008 Wenchuan earthquake, the April 2013 Lushan earthquake, and the August 2017 Jiuzhaigou earthquake. The revealed anomalies associated with the Wenchuan and Lushan earthquakes were distributed along the main faults, but that associated with the Jiuzhaigou earthquake was distributed around the epicenter and did not stay relevant to the seismogenic structures. Maeda and Takano [15], [16] have also studied the MBT anomalies related to the February 2004 Morocco earthquake and the May 2008 Wenchuan earthquake. It was uncovered that anomalous pixels of the Wenchuan earthquake were primarily distributed along the Longmenshan faults (LMSFs), but those of the Morocco earthquake were scattered around the epicenter zone. In the research of Yang and Guo [21], the most significant anomalies related to 2010 Baja California earthquake occurred primarily on both sides of the fault line, but not all were concentrated at the epicenter zone. These results suggest the difficulty in describing uniformly the seismic MBT anomaly with similar or certain abnormal characteristics in a limited area, and that different types of earthquakes and even seismogenic preparation environment may have a profound impact on the satellite-observed MBT anomaly.

The present research first uncovered and discussed the characteristics and uncertainties of multitemporal seismic MBT anomalies before, during and after the Wenchuan earthquake in May 2008, the Yushu earthquake in April 2010, the Lushan earthquake in April 2013, and the Nepal Gorkha and Dolakha earthquakes in 2015, by using different removal methods of historical background. Cross-comparisons of the frequency and polarization of the MBT data were conducted, and the causes of the induced inconsistencies and uncertainties were analyzed based on remote sensing physics. Then, the spatiotemporal evolutions of MBT anomalies and the preparation mechanisms associated with the four earthquake cases were discussed carefully. Some ideas about selection and usage of multitemporal MBT data for seismic anomaly monitoring were suggested, and the applications as well as limitations in the research itself were objectively pointed out.

II. METHODOLOGY

Preseismic anomalies are always weak signals in contrast to the strong background field, which is strongly influenced by seasonal factors, topography, vegetation condition, and meteorology. To quantitatively analyze the possible thermal anomalies related to earthquakes, the image-difference method was introduced to identify abnormal signals in the same region over a long time series of satellite observations [3], [10], [25], [26]. Such method aims to eliminate the tendency changes within satellite images by removing a background (also a reference field) based on multiyear data, thereby underlining the abnormal information that exceeds the predefined threshold.

In this research, we used the spatiotemporally weighted two step method (STW-TSM) [22] to retrieve the time series of seismic MBT anomaly and made comparison with different background-removal methods. The principle of STW-TSM is to obtain the basic residuals and the cleaned MBT residuals of ground-surface MBT in two separate steps by removing a temporal and a spatial weighting background, respectively. A brief description of the method is as follows.

A. First Step

The first step is to remove the inherent stable and general trend from satellite MBT observations with a temporally weighted background

$$T_w(x,y,t_\xi) = \frac{\sum_{i=1}^{n} \left[\exp(-\frac{(\varphi_i-\xi)^2}{D_1^2}) \cdot T(x,y,t_i)\right]}{\sum_{i=1}^{n} \exp\left[-\frac{(\varphi_i-\xi)^2}{D_1^2}\right]} \quad (1)$$

$$\triangle T(x,y,t_\xi) = T(x,y,t_\xi) - T_w(x,y,t_\xi) \quad (2)$$

where φ_i stands for any nonseismic year with a serial number i, ξ represent the earthquake year. D_1 is an adjustable coefficient and refers to the maximum year interval between shock year and all nonearthquake years of used data. $T(x,y,t_i)$, and $T(x,y,t_\xi)$ are the values of pixel (x,y) on the date of t_i and t_ξ, respectively. t_i and t_ξ represent the same date in the nonearthquake year i and the earthquake year ξ, respectively. $T_w(x,y,t_\xi)$ is the weighted value for the shock year based on all $T(x,y,t_i)$, and $\Delta T(x,y,t_\xi)$ is the basic residual value of pixel *(x, y)* on date t_ξ.

B. Second Step

The second step is to restrain random noise with a spatially weighted background on the basis of the first step's residual images

$$T_m(x,y,t_\xi) = \frac{\sum_{k=1}^{p} \left[\exp(-\frac{(i_k-x)^2+(j_k-y)^2}{D_2^2}) \triangle T(i_k,j_k,t_\xi)\right]}{\sum_{k=1}^{p} \left[\exp(-\frac{(i_k-x)^2+(j_k-y)^2}{D_2^2})\right]}$$
$$(3)$$

$$\triangle\triangle T(x,y,t_\xi) = \triangle T(x,y,t_\xi) - T_m(x,y,t_\xi) \quad (4)$$

where D_2 is an adjustable coefficient and stands for the diagonal length of the actual study area, and W_k is the spatial weight of pixel (i_k, j_k). $T_m(x,y,t_\xi)$ means the interpolated value of far-field meteorological impact on pixel (x, y) in shock day t_ξ, and $\Delta T(i_k, j_k, t_\xi)$ represents the value of periphery pixel (i_k, j_k). $\Delta\Delta T(x,y,t_\xi)$ is termed as the cleaned residual value of pixel (x, y) in day t_ξ, which is considered to be seismicity related and can be adopted subsequently to conduct a time-series analysis.

Meanwhile, to fill in the missing area of the study area due to the periodic satellite swath, a preprocessing of sliding window is introduced in the STW-TSM by using the average MBT 14

days before and 14 days after a certain date [22]. The complete residual MBT images are used to analyze the multitemporal evolution and explore the possible causes of the earthquake anomaly.

III. Earthquake Cases and Data Sources

A. Selected Earthquake Cases

This research chose the May 2008 Wenchuan earthquake and the April 2013 Lushan earthquake occurred in Sichuan Province, China, the April 2010 Yushu earthquake occurred in Qinghai Province, China, and the 2015 Nepal earthquake sequence happened in Central Nepal, as typical case studies, to make comparisons and to search for the inconsistencies due to different method used, data used, and case studies. The driving forces of the selected four earthquake cases were similar, but their seismogenic mechanisms have characteristic differences, which is worth a comparative analysis.

The May 12, 2008 Wenchuan earthquake occurred in the LMSFs region at the junction of the eastern Tibetan Plateau and the western Sichuan Basin, with a magnitude of Mw 7.9 and the epicenter located at 31.02° N, 103.37° E [27]. The focal depth was about 19.0 km, and numerous aftershocks of magnitude greater than Mw 5.0 appeared along the LMSFs from the mainshock day to the end of May 2008 (from USGS), forming the Wenchuan earthquake sequence. This violent earthquake generated a surface rupture zone more than 240 km long along the Beichuan fault and another surface rupture zone more than 70 km long along the Pengguan fault [28]. The local elevation varies sharply from a few hundred meters to a few thousand over a distance less than 50 km, making the terrain very complex and dramatically changing.

Near the southwest of the epicenter of the Wenchuan earthquake, another large earthquake with magnitude of Mw 6.6 occurred also in the LMSFs region on April 20, 2013, i.e., Lushan earthquake, also known as the Ya'an earthquake. The epicenter of this earthquake located at 30.30° N, 103.00° E with a depth of about 13.0 km [29]. It was believed that the occurrences of the Wenchuan earthquake may have contributed to the formation of the Lushan earthquake [30], but the comparative analysis of the focal mechanics mechanism, rupture process, spatial distribution of aftershocks and surface rupture suggested that these two earthquakes are relatively independent seismic events [31].

The aforementioned two earthquakes both appeared at the junction of east Bayan Har block and South China block, and the Yushu earthquake occurred at southern edge of the Bayan Har block on April 13, 2010, with a magnitude of Mw 6.9 and the epicenter located at 33.17° N, 96.55° E. This earthquake was mainly due to the eastward movement of Kunlun block leading to the sinistral slip of Garzê–Yushu Fault [32], the initial cause and the energy source of these three large earthquakes was the Indian plate's wedging in Qinghai–Tibet Plateau, resulting in the movement and collision of the interior blocks and subblocks.

On the southern rim of the Himalayan Mountains, where the Indian Plate met the Qinghai–Tibet Plateau, an Mw 7.8 thrust earthquake occurred in Gorkha, central Nepal on April 25, 2015, which was previously identified as a high-seismic-hazard zone

TABLE I
MAJOR CHARACTERISTICS AND PERFORMANCE OF AMSR-E

Frequency (GHz)	Ground IFOV scan×along track (km)	Band width (MHz)	NEΔT (K)
6.9	43×75	350	0.34
10.7	29×51	100	0.7
18.7	16×27	200	0.7
23.8	18×32	400	0.6
36.5	8×14	1000	0.7
89.0	4×7	3000	1.2

due to the active change of the crust stress field. According to the USGS, the epicenter of the Gorkha event was located at 28.18° N, 84.72° E with a depth of 18 km. This hazardous earthquake was followed by a series of large aftershocks, including a Mw 7.3 Dolakha earthquake on May 12, 2015. The earthquake sequence was caused by the northeastward subduction and squeezing of the Indian plate beneath the Himalayan tectonic belt at the junction of the Indian plate and the Eurasian–Asian plate, leading to the long-term accumulated crustal stress reaching the shear strength of the thrust faults and causing a sudden slip [33].

B. Satellite MBT Data

When selecting MBT data, it was first considered whether the operation time of the satellite covered the moment of earthquake occurrence and whether the data coverage could provide enough time series of radiation information before and after the earthquake to satisfy the data requirement of historical background construction. Therefore, AMSR-E instrument onboard Aqua satellite and MWRI instrument onboard FY-3B satellite stood out from the crowd to provide MBT data for investigating the four selected earthquake cases.

The AMSR-E was one of the highest performing instruments provided to Aqua satellite, which was launched in 2002 by the National Aeronautics and Space Administration (NASA). This device was used to observe the earth surface at six microwave bands (6.9, 10.7, 18.7, 23.8, 36.5, and 89 GHz) with dual polarization (V and H) [34]. The temporal coverage of AMSR-E data was from 2002 to 2011, and covered the shock times of the Wenchuan earthquake in 2008 and the Yushu earthquake in 2010. The major characteristics and performance of the instrument are described as Table I. The dataset used in the study are AMSR-E Level-2A product (AE_L2A, descending mode), which are resampled to spatial resolutions ranging from 5.4 to 56 km (corresponding to six channels from 89 to 6.9 GHz). Each file of the data contains daily 50-min half-orbit swath brightness temperatures, which is packaged with quality information as well as geolocation.

The MWRI instrument was onboard the second-generation Chinese meteorological satellite (FY-3B) and provided microwave radiative observations of the earth's surface at microwave frequencies of 10.7, 18.7, 23.8, 36.5, and 89.0 GHz with dual-polarization modes [35]. The temporal coverage of the FY-3B MWRI data was from 2010 to 2019, satisfying the data requirements of seismic-anomaly monitoring on the Lushan earthquake in 2013 and the Nepal earthquake sequence in 2015. The main characteristics and performance of FY-3B MWRI are shown in Table II. The dataset used of FY-3B MWRI are Level-1

TABLE II
MAJOR CHARACTERISTICS AND PERFORMANCE OF FY-3B

Frequency (GHz)	Ground IFOV scan×along track (km)	Band width (MHz)	NEΔT (K)
10.7	51×85	180	0.5
18.7	30×50	200	0.5
23.8	27×45	400	0.5
36.5	18×30	900	0.5
89.0	9×15	2300	0.8

product (GBAL_L1, descending mode), with spatial resolutions ranging from 10 to 73 km (corresponding to five channels from 89 to 10.7 GHz). The data packages also contain information of geolocation, calibration, and data quality.

IV. RESULTS AND DISCUSSION

A. Background-Removal Method

Seismic thermal anomaly can be defined as the difference between what occurred in the shock year and what was expected according to an existing long-term trend (background). Based on this idea, many researchers have calculated the differential values between the seismic year data and the long-term average value by using numerous kinds of remote-sensing data to detect potential anomaly related to some large earthquakes [9], [36]–[38]. However, the problem lies in which the results of anomaly extraction largely depend on the establishment and removal of background field; the spatiotemporal pattern and the effectiveness of noise removal are sensitive to the processing of influencing factors over time. Thus, great uncertainty may exist in the retrieved anomalous information.

Theoretically, passive satellite microwave images contain various pieces of heterogeneous radiative information within the satellite footprint and reflect the energy exchange of the earth's surface. The observations are strongly influenced by the physical properties of coversphere and short-term variable meteorology in time and space. Taking the May 2008 Wenchuan earthquake, the April 2010 Yushu earthquake, the April 2013 Lushan earthquake, and the 2015 Nepal earthquake sequence as examples, we considered using two different removal methods of background field to extract the related seismic MBT anomalies, i.e., the average background field and the spatiotemporally weighted background field [22]. The average background assumes that the influential factors, including seasons, surface coverage, local weather, and topography exhibit an unchanged state over time or uniform distribution in space. While the spatiotemporally weighted background considers that the variation trends of each influencing factor is dynamic over time or variable in space, multitemporal data of different year and pixels inside the study area are assigned with different weights according to their time intervals with the shock year and the Euclidean geospatial distance away from the epicenter, respectively. The results of revealed multitemporal MBT anomalies before, during and after the four earthquake cases using two different background-removal methods are shown in Fig. 1.

According to Fig. 1, the differences in amplitude and spatial distribution of MBT anomalies related to the four selected earthquake cases are very significant. As for the Wenchuan earthquake and the Nepal earthquakes, the results from averaged background show many large-scale positive and negative MBT anomalies, and some obvious positive anomalies appear at the edges of the study area and in the central study area, making the extracted results difficult to recognize. However, the widely varying range of anomaly values in the study area may indicate that some non-earthquake disturbances (e.g., terrain and vegetation) are not effectively eliminated; the results from spatiotemporally weighted background can reduce the interference to some extent. As for the Yushu earthquake and the Lushan earthquake, the results from averaged background can reflect a certain positive MBT anomalies near the epicenters, but compared with that from spatiotemporally weighted background, the revealed anomalies appeared to be partially missing and the degree of anomalies was not significant.

In addition, the result of Nepal earthquakes from averaged background shows obvious stripe traces of satellite swath possibly due to the coverage of multitemporal data, which illustrates the importance of the preset sliding window processing. By comparing the results of these four cases, it is evident that the results from spatiotemporally weighted background show a better aggregation of MBT anomalies. And significant positive MBT anomalies primarily occur near the epicenter and the fault lines with a more pronounced degree of abnormality. Besides, the distribution of value range in the study area is more uniform, so the positive anomalies related to earthquakes can be highlighted. In summary, the comparison results suggest that different background removal method can reveal different spatiotemporal patterns and amplitudes of anomaly, which are bound to have a profound impact on the cognition of seismic anomalies.

B. Frequency of Data Used

In this section, by employed the spatiotemporally weighted background, MBT anomalies of the four earthquake cases were calculated using MBT data with different bands, to analyze and discuss the uncertainties induced by wavelength and spatial resolution. The MBT data derived from AMSR-E instrument with 6.9, 10.7, 18.7, and 36.5 GHz at H polarization were used for the May 2008 Wenchuan earthquake and the April 2010 Yushu earthquake, and MBT data from FY-3B MWRI instrument with 10.7, 18.7, 23.8, and 36.5 GHz at H polarization were selected for the April 2013 Lushan earthquake, and the 2015 Nepal earthquakes. The performance in thermal radiation sensitivity of the selected bands are all greater than 1 K while the viewing angles of all the selected bands are the same (54.8° for AMSR-E and 45° for MWRI).

Fig. 2 shows the result of four bands on May 11 and May 12, 2008 of the Wenchuan earthquake, on April 5 and April 13, 2010 of the Yushu earthquake, on April 18 and April 19, 2013 of the Lushan earthquake, and on April 24 and May 11, 2015 of the Nepal earthquakes. It can be easily found that the MBT anomalies on the same day significantly changed with the increasing of frequency. Taking the result of Wenchuan earthquake and Nepal earthquakes as an example, the results with lower frequency (such as 6.9 and 10.7 GHz) have more significant abnormality but less detailed information in a spatial pattern, whereas that with higher frequency (such as 23.8 and
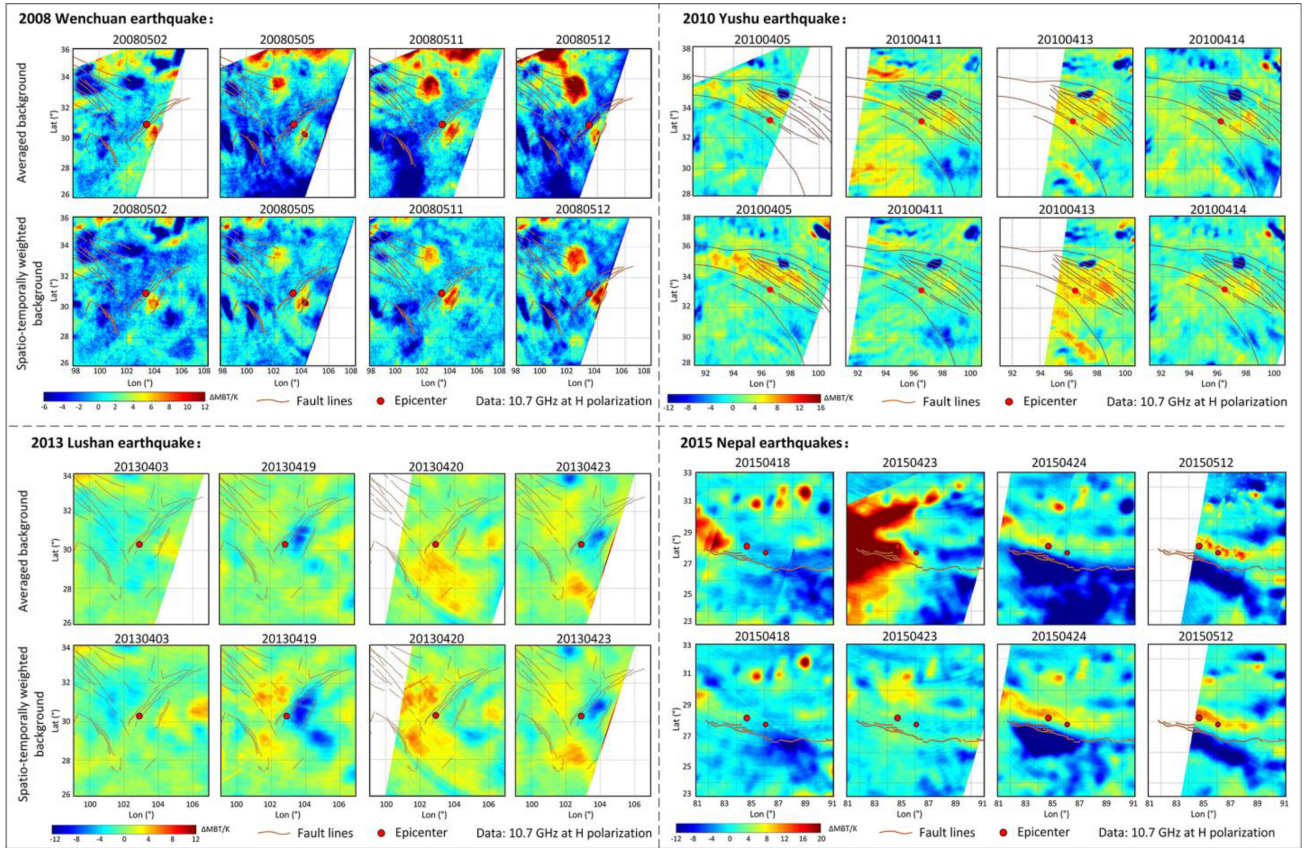
Fig. 1. Revealed MBT anomalies of the 2008 Wenchuan earthquake, the 2010 Yushu earthquake, the 2013 Lushan earthquake, and the 2015 Nepal earthquakes based on two different backgrounds.

36.5 GHz) can show more localized variable information and clearer outlines of the obtained anomalies but less intense MBT abnormities in the study area. As for the other two cases, it can be found that some positive and negative anomalies showed significant inconsistency with frequency. For instance, the result of 2010 Yushu earthquake exhibited most significant positive abnormity at 10.7 GHz around the epicenter on the shocking day (April 13), and the degree of positive anomaly south of the epicenter increased with frequency, which is contrary to the result of Wenchuan earthquake. The result of 2013 Lushan earthquake presented enhanced intensity with frequency in the area northeast of the epicenter on April 18, but the anomaly northwest of the epicenter on April 19 showed decreased intensity with frequency and exhibited most obvious abnormity at 10.7 GHz.

According to microwave remote sensing physics [24], [39], for an electromagnetic wave propagating in lossy medium, its penetration depth (δ) is primarily related to the wavelength (λ) and the physical property (dielectric, ε) of the medium

$$\delta = \lambda \Big/ \sqrt{2\pi^2 \varepsilon' \left[\sqrt{1 + \left(\frac{\varepsilon''}{\varepsilon}\right)^2} - 1 \right]} \qquad (5)$$

where ε' and ε'' refer to the real and imaginary parts of ε, respectively.

Therefore, the attenuation of microwave radiation is inversely proportional to the wavelength, and the penetration depth through the earth's surface media and the penetration efficiency through the atmosphere of microwave radiation are proportional to the wavelength. As regards the aforementioned phenomenon, the microwave radiative signals with high frequency have shorter wavelength and higher spatial resolution. Accordingly, the seismic anomalies at these bands can reflect only the thermal radiation of a very shallow subsurface owing to its penetration of land surface, and the transmission of radiative signals to satellite sensor are more easily polluted and weakened by atmospheric water vapor and small-scale meteorological disturbances. Additionally, the higher spatial resolution enables the detection of anomalies at very small scales so that the result with high frequency shows scattered hot spots of positive MBT anomalies. Conversely, the transmission of microwave radiation with low frequency (such as 6.9 and 10.7 GHz) is believed to be independent of atmospheric water vapor [24], so the result reveals greater amplitude of anomalies. The seismic abnormal signals received by satellite sensors at these frequencies can also contain more radiative information from much deeper subsurface owing to their penetrability. Many small-scale anomalies may be smoothened during the sampling process owing to the rough spatial resolutions of lower frequency data; thus, the result can only exhibit larger scale of abnormality.
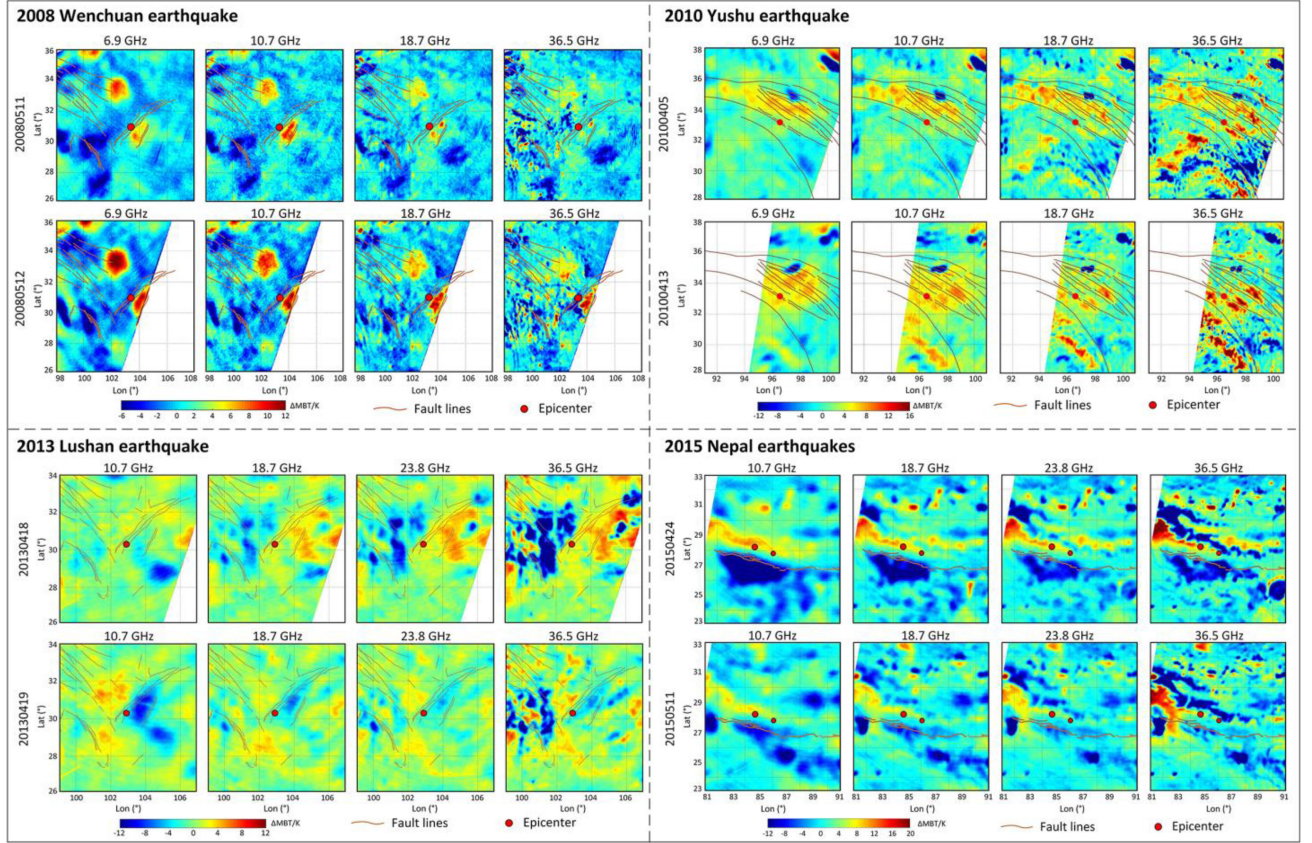
Fig. 2.   Revealed MBT anomalies with four different bands at H polarization related to the four earthquake cases.

C. *Polarization of Data Used*

To explore the impact of polarization mode on the spatiotemporal pattern of seismic anomaly, the multitemporal MBT anomalies related to the four selected earthquake cases were extracted accordingly with AMSR-E data and MWRI data at 10.7 GHz, and the results are shown in Fig. 3. The positive and negative MBT anomalies of all the four earthquakes at H and V polarizations have similar distribution in space and evolution over time, but the amplitude and the spatial scales of MBT anomaly at H polarization are greater than that at V polarization, especially for the positive anomalies of the Wenchuan earthquake in the central study area and the area about 300 km northwest away from the epicenter, the positive anomalies of the Yushu earthquake in the area northwest of the epicenter, the positive anomalies of the Lushan earthquake north of the epicenter, and the positive anomaly along the Himalayas and the negative anomalies in the Gangetic Plain of the Nepal earthquakes. The differences in degree of abnormality revealed in Fig. 3 is similar to a previous result [18] indicating that H polarization is more sensitive to same disturbance of land surface under the same observation conditions.

Under actual observation conditions, the brightness temperature observed by the microwave satellite instrument at a given frequency and at a given incidence angle can be expressed by a microwave radiative transfer model proposed in [40]. The earth's surface is considered to be heterogeneous that three layers

including soil, vegetation, and atmosphere contribute all of the observed radiation. The equation can be described as

$$
\begin{aligned}
T_{Bp} = T_u + \exp(-\tau_a)[&\{T_d(1 - e_{Sp})\exp(-2\tau_c)\} \\
&+ \{e_{Sp}\, T_S \exp(-\tau_c) \\
&+ T_C(1 - \omega_p)[1 - \exp(-\tau_c)][1 + (1 - e_{Sp})\exp(-\tau_c)]\}]
\end{aligned}
\tag{6}
$$

where T_{Bp} is the satellite observed brightness temperature at polarization p (V or H), T_u is the upwelling atmospheric emission, T_d is the downwelling atmospheric and space-background emission at the top of the vegetation. τ_a is the atmospheric opacity while τ_c stands for vegetation opacity. T_S denotes the physical temperature of soil and T_C is the vegetation temperature. e_{Sp} is soil emissivity and ω_p is vegetation single scattering albedo.

Generally, the vegetation and underlying soil are at close to the same physical temperature T_e, and canopies are assumed to be the same, thus ω_p can be set to zero. Then, based on (6), the difference of brightness temperature at two polarizations can be calculated as following:

$$
\begin{aligned}
T_{Bv} - T_{Bh} = \exp(-\tau_a)[&\{T_d(e_{Sh} - e_{Sv})\exp(-2\tau_c)\} \\
&+ T_e \exp(-\tau_c)\{(e_{Sv} - e_{Sh}) \\
&+ [1 - \exp(-\tau_c)][(e_{Sh} - e_{Sv})]\}].
\end{aligned}
\tag{7}
$$

For a certain observation, physical temperature T_e, vegetation opacity τ_c, and atmospheric opacity τ_a are definite without
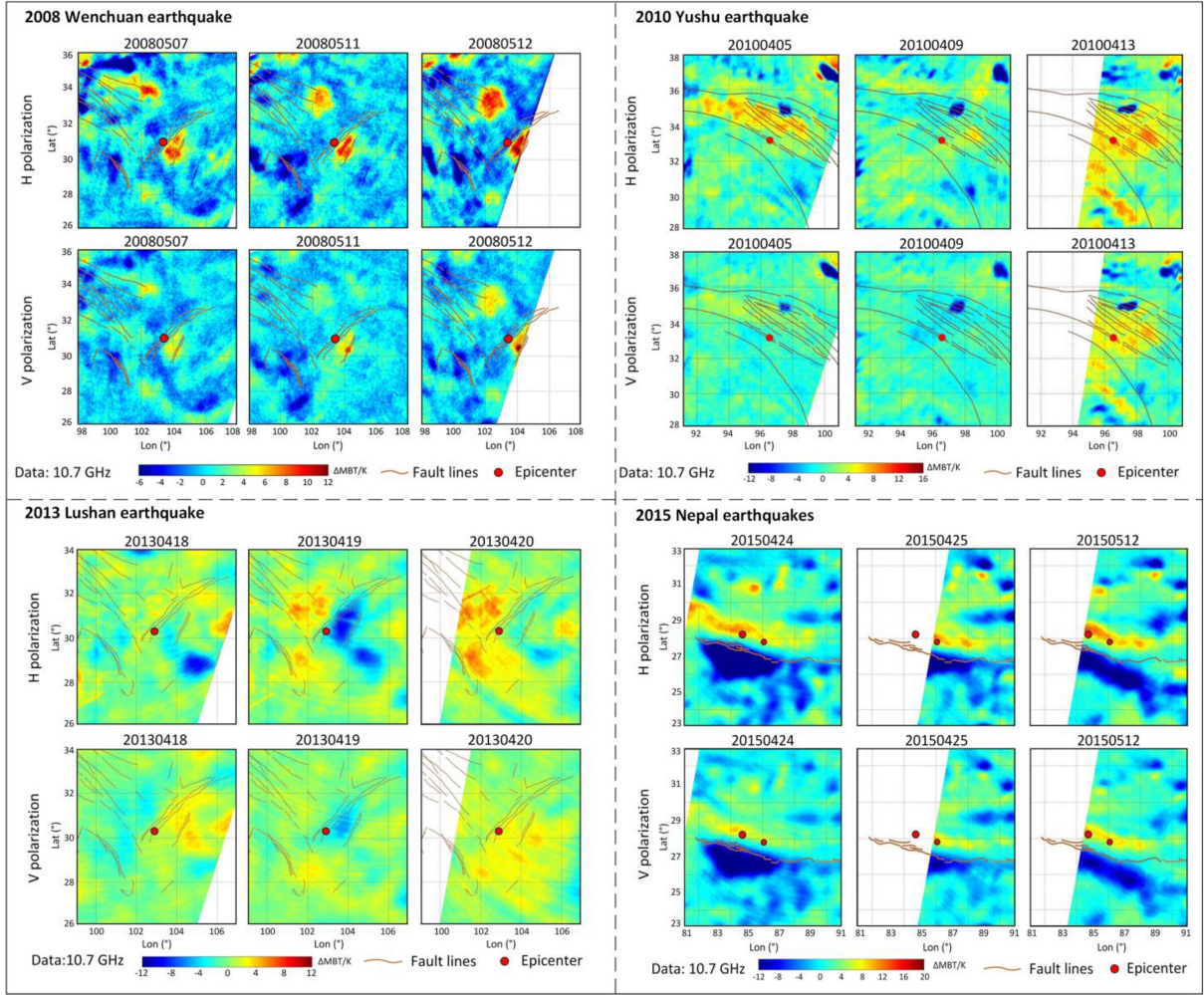
Fig. 3. Revealed MBT anomalies at H and V polarization related to the four earthquake cases.

polarization difference. Thus, according to (7), the polarization inconsistency between the bright temperatures can be mainly attributed to the emissivity of the soil layer e_{Sp}.

The Fresnel equations suggest that the emissivity e_{Sp} of land surface is relevant to the incidence angle (θ) and dielectric properties (ε) [39]. In order to apply the Fresnel equations to the analysis, smooth and homogeneous soil surfaces need to be assumed, otherwise too many parameters will be introduced to make the analysis impossible to control variables. The incidence angle θ used in the microwave satellite sensor is fixed as 54.8° in AMSR-E [34] and 45° in FY-3B MWRI [35]. For H & V polarization with a given frequency, the emissivity e_{Sp} is expressed as following equations:

$$e_{Sh} = 1 - \left| \frac{\cos(\theta) - \sqrt{\varepsilon - \sin^2(\theta)}}{\cos(\theta) + \sqrt{\varepsilon - \sin^2(\theta)}} \right|^2 \qquad (8)$$

$$e_{Sv} = 1 - \left| \frac{\varepsilon \cos(\theta) - \sqrt{\varepsilon - \sin^2(\theta)}}{\varepsilon \cos(\theta) + \sqrt{\varepsilon - \sin^2(\theta)}} \right|^2. \qquad (9)$$

Apparently, the dielectric property ε of the soil surface plays a decisive role in emissivity e_{Sp} and, thus, in the satellite-observed MBT. This part mainly discusses the sensitivity of MBT of

the single polarization to the change of surface parameters. Therefore, the change value of e_{Sp} and MBT with different polarization relative to its original value can be calculated using (8) and (9). And according to the Rayleigh–Jeans law, MBT of an object is related to its physical temperature T_e and emissivity e_{Sp}, so that the response of ΔMBT to dielectric change can be simply simulated by the following derived equations:

$$\Delta T_{Bh} = \left(\left| \frac{\cos\theta - \sqrt{\varepsilon_1 - \sin^2\theta}}{\cos\theta + \sqrt{\varepsilon_1 - \sin^2\theta}} \right|^2 \right.$$
$$\left. - \left| \frac{\cos\theta - \sqrt{\varepsilon_2 - \sin^2\theta}}{\cos\theta + \sqrt{\varepsilon_2 - \sin^2\theta}} \right|^2 \times T_e \right) \qquad (10)$$

$$\Delta T_{Bv} = \left(\left| \frac{\varepsilon_1 \cos\theta - \sqrt{\varepsilon_1 - \sin^2\theta}}{\varepsilon_1 \cos\theta + \sqrt{\varepsilon_1 - \sin^2\theta}} \right|^2 \right.$$
$$\left. - \left| \frac{\varepsilon_2 \cos\theta - \sqrt{\varepsilon_2 - \sin^2\theta}}{\varepsilon_2 \cos\theta + \sqrt{\varepsilon_2 - \sin^2\theta}} \right|^2 \times T_e \right) \qquad (11)$$
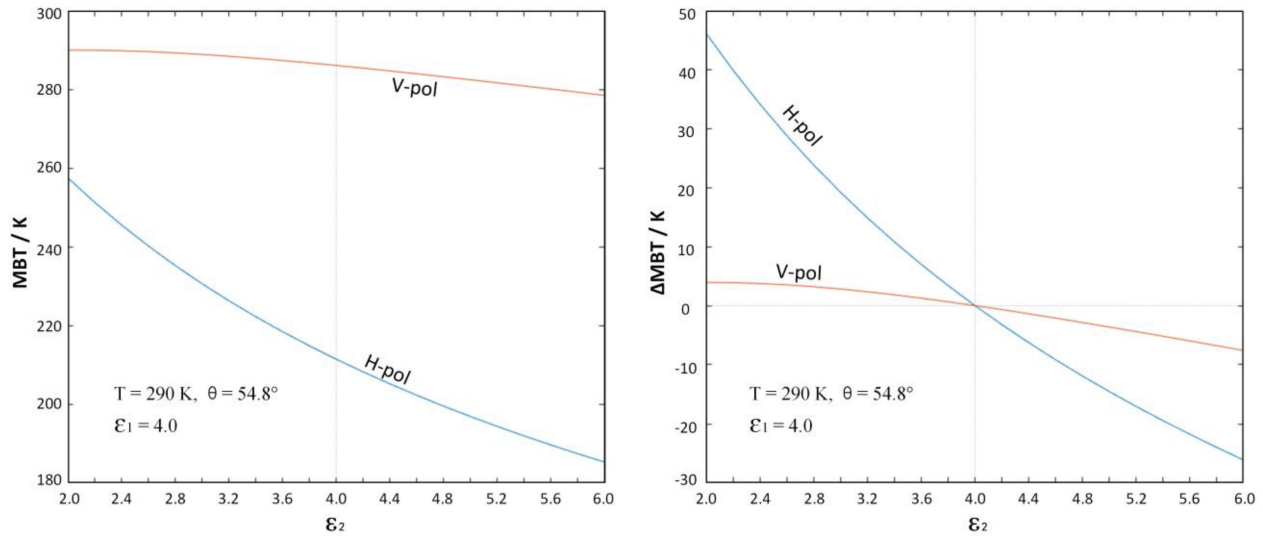
Fig. 4. Simulation of changes in MBT (left) and ΔMBT (right) with dielectric constants at H and V polarization. The horizontal axis ε_2 represents the changed dielectric constant and ε_1 refers to preset value of dielectric constant.

where ε_1 is the original value of dielectric constant, ε_2 is the changed dielectric constant, and ΔT_{Bp} stands for the change in MBT at V or H polarization mode.

Considering the actual observed temperature, the physical temperature T_e of land surface at the time of satellite transit (about 18:00 UTC) was assumed to be 290 K, and the incidence angle θ of satellite sensor was selected as 54.8° (for AMSR-E). Simply, the original value of dielectric constant of ground surface was set to 4.0 (average permittivity of dry soil), then a numerical simulation was conducted to explore the change in MBT under different polarization modes caused by the change in dielectric constant. In the simulation, only the real part of the complex permittivity was considered. The imaginary part mainly reflects the loss of the dielectric constant, and for dry soil, rocks and minerals on the earth's surface, the imaginary part contributes less to the module of the complex permittivity, so that the influence of the dielectric loss is often negligible.

Fig. 4 shows the result of the simulation. Obviously, the absolute values of MBT at V polarization are bigger than that at H polarization with the same dielectric constant (left subgraph), which fits with actual situation that satellite MBT observation at V polarization is generally higher than that at H polarization. As regards the change in MBT caused by dielectric constant variation (right subgraph), Fig. 4 shows that the values of ΔMBT at H polarization are bigger than that at V polarization with the same dielectric constant, which is consistent with Fig. 3 that changes in MBT (i.e., MBT anomaly) at H polarization and is more significant than that at V polarization under the same condition. Therefore, it is clear that the polarization mode of satellite MBT data introduces uncertainty in the intensity degree of the results, thereby also affecting the spatiotemporal pattern of multitemporal seismic anomaly. It should be pointed out that this simulation is a simplistic and qualitative result, and many auxiliary data and empirical parameters are needed to accurately quantify the polarization difference of the brightness temperature. From the comparison results, it is suggested that

MBT data at H polarization is better than at V polarization in detecting changes in seismic thermal radiation.

D. Mechanism of Earthquake Preparation

Enhanced microwave radiations occurring near the epicenter or along the faults zone preceding some large earthquakes have been frequently reported, and the uncertainties in the characteristics of these anomalies are bound to confer difficulties in the identification and interpretation of seismic anomalies. Thus, the scientific cognition of seismic-anomaly features still needs a large number of case studies and summaries from the perspective of multitemporal analyses. Given that the current research does not well combine the spatiotemporal evolution of MBT anomalies with the seismogenic process of large earthquakes, we selected the four typical earthquake cases to study the impact of seismogenic preparation model and the aftershocks on the spatiotemporal patterns of the obtained MBT anomalies. Fig. 5 shows the multitemporal MBT anomalies associated with the four earthquake cases in several critical days. Fig. 6 exhibits the earthquake frequency before and after the mainshock, and Fig. 7 presents the average MBT and average MBT anomalies around the epicenter (with a $2° \times 2°$ range) from months before and months after the mainshock of the four cases.

The May 12 Wenchuan earthquake is considered to result from the southeastward motion of the Bayan Har block and the strong blocking by the Sichuan Basin such that the elastic strain on the structure belt slowly accumulates and suddenly exceeds the sliding friction strength of the thrust [41]. In the final preparation period of the Wenchuan earthquake, the crustal stress that accumulated at the hypocenter zone was strengthened dramatically, and the LMSFs zone first became the prime high-stress-concentration zone. According to the earthquake frequency map [see Fig. 6(a)], there was no foreshock before the Wenchuan earthquake, so the energy accumulation in the stress concentration area was deservedly much greater. Consequently,
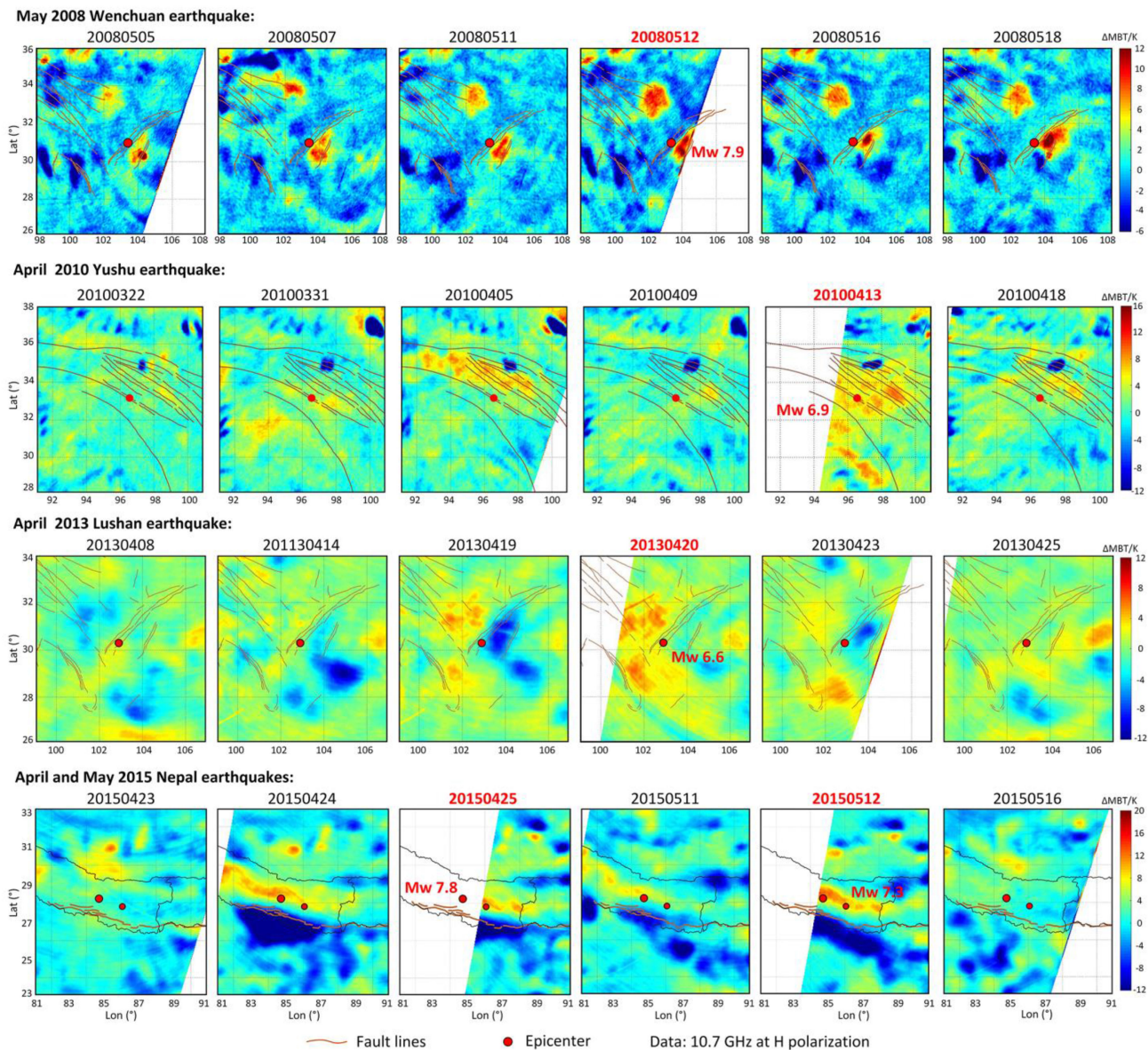
Fig. 5. Evolutions of MBT anomalies on the featured dates before, during, and after the four earthquake cases.

the significant positive MBT anomaly first appeared east close to the upcoming epicenter, and the MBT and its variation (MBT anomaly) have shown an increasing trend since about two weeks before the mainshock [see Fig. 7(a)]. With the Bayan Har block maintaining eastward movement, the strong blocking of the Sichuan Basin gave the Bayan Har block a tendency to strike-slip northeast and to be resisted by the West Qinling block. As a result, the northwest anomaly area (about 300 km away from the epicenter) became the secondary high-stress-concentration zone. Therefore, the positive MBT anomalies occurred a little later than the central anomaly. After the May 12 mainshock, the prime high stress concentration at the junction of the Bayan Har block and South China block migrated northeastward along LMSFs, following by numerous aftershocks [see Fig. 6(a)], thereby shifting the geolocation of the central MBT anomaly to the northeast with aftershocks. With diminishing of the large

aftershocks, the time series of MBT anomaly around the epicenter decreased subsequently [see Fig. 7(a)].

The April 2013 Lushan earthquake occurred in the southwest section of the LMSFs zone on the eastern margin of the Qinghai–Tibet Plateau, which was a thrust earthquake and had the same focal mechanism as the Wenchuan earthquake, but with a smaller dextral strike-slip component [29]. The stress concentration zone preceding this earthquake might appeared at the southern tail region caused by the continuous compression of the Bayan Har block; thus, the positive anomaly occurred to the north of the junction of the Xianshuihe faults and LMSFs zone, and the average MBT anomaly around the epicenter achieved peak right on the shocking day and one day before [see Fig. 7(c)]. In Fig. 6(c), few aftershocks were recorded after the mainshock, which indicated that these areas around the epicenter may still be locked and the stress was not fully released [30]. Therefore,
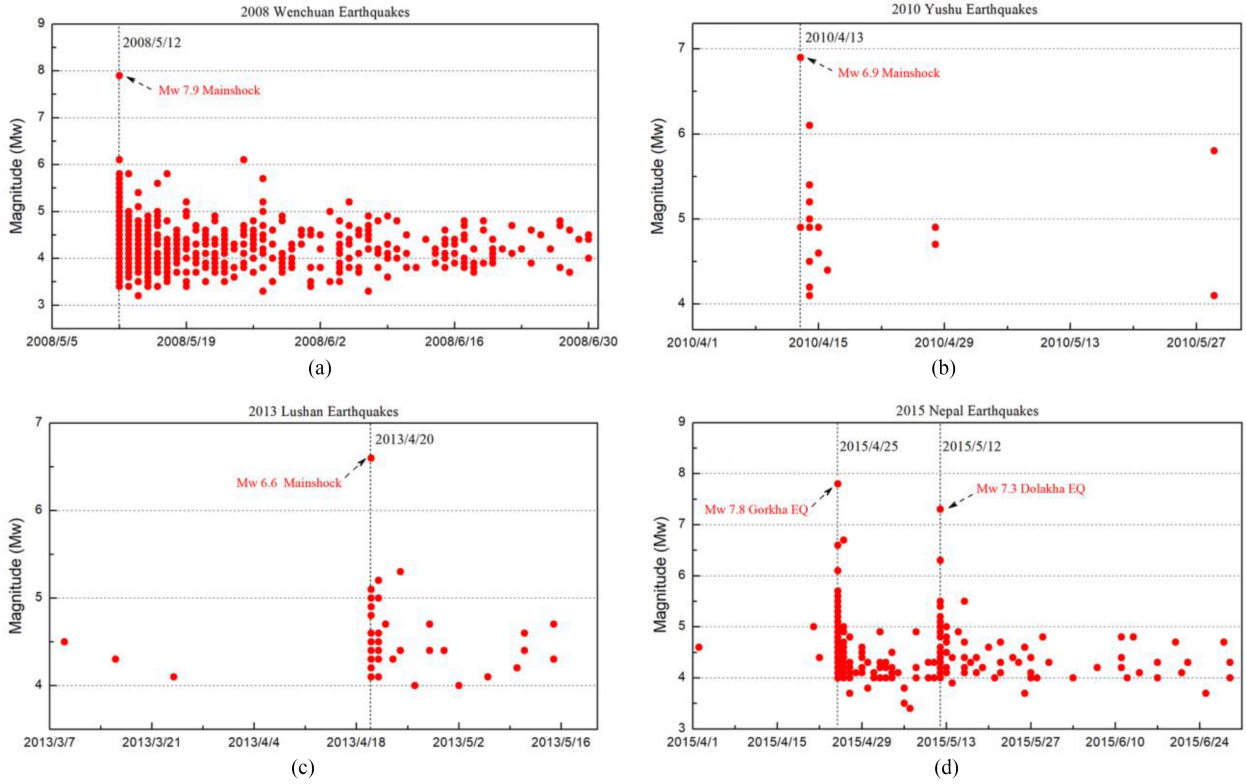
Fig. 6.   Scatter diagrams of earthquake frequency before, during, and after the four earthquake cases.
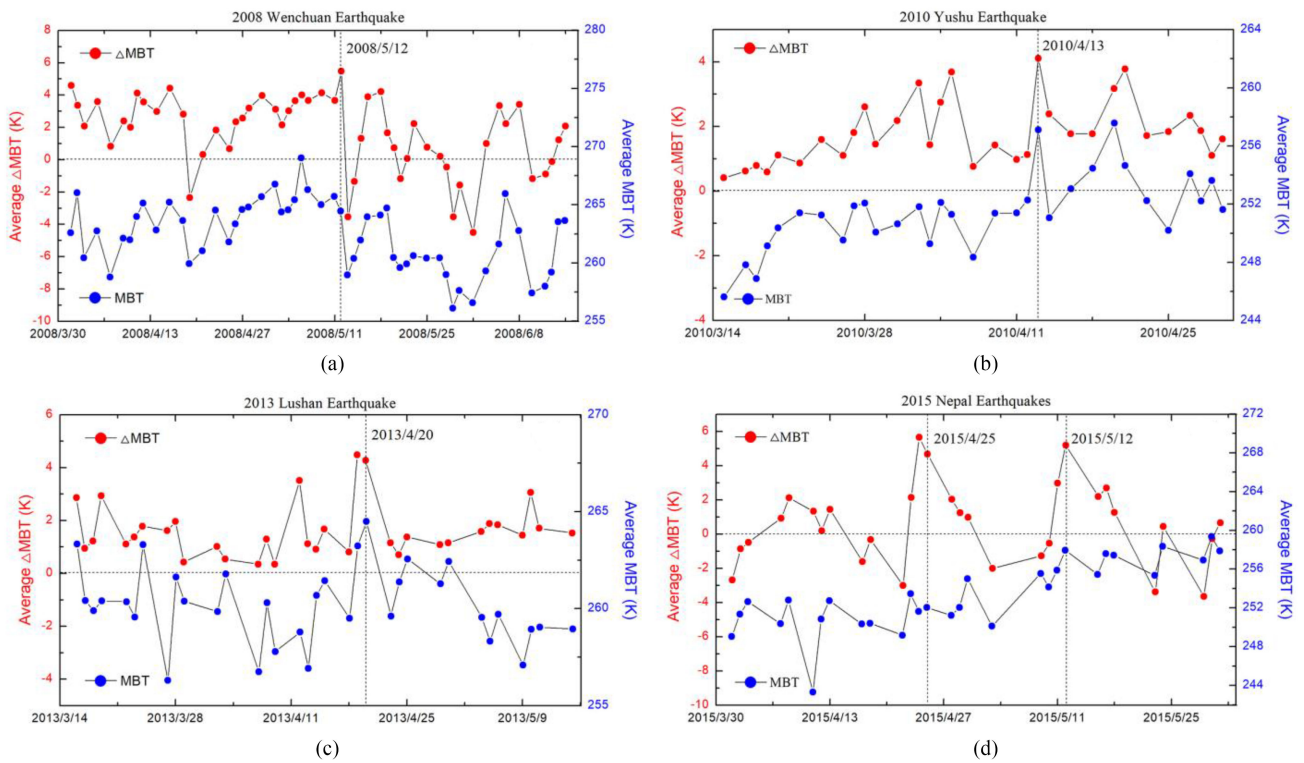

Fig. 7.   Time series of average MBT anomaly and MBT observation around the epicenters of the four earthquake cases.

the abnormal phenomenon did not appear to be metastatic like the 2008 Wenchuan earthquake sequence.

The 2010 Yushu earthquake was another major earthquake under the background of the Indian plate pushing northward, the uplift of the Qinghai–Tibet plateau and the eastward extrusion of the secondary Bayan Har active block [42]. The surface rupture pattern of this earthquake showed that the Garzê–Yushu Fault was dominated by a pure left-lateral faulting. The subblocks near the suture zone collided and moved with each other, and the East Kunlun fault zone and the Yushu–Garzê–Xianshuihe fault zone slipped to the eastern margin with relatively weak constraint conditions, accompanied by the block movement [43]. Therefore, the most significant region of MBT anomalies concentrated on the northern faults zone before the earthquake (April 5) and, then, overlapped with the epicenter on the mainshock day (April 13). In Fig. 7(b), the time series of average MBT anomaly around the epicenter shows a process of rising and then falling, which corresponds to the dynamic process of stress accumulation before the earthquake and stress release after the earthquake.

The Mw 7.8 Gorkha mainshock and the Mw 7.3 Dolakha aftershock were caused by the northeastward subduction and squeezing of the Indian plate to the Himalayan tectonic belt [33], [44]. During the late seismogenic period of the Mw 7.8 Gorkha mainshock, the long-term-accumulated crustal stress at the Himalayan tectonic belt resulted in a principal stress concentration zone along the Himalayas, and the positive MBT anomaly was uncovered as being strip shaped on April 24 and April 25, 2015, and the average MBT anomaly also reached its maximum on these two days [see Fig. 7(d)]. After the Gorkha main shock, most of the accumulated stresses were released, so the central study area in this period became temporally calm. With the Mw 7.3 Dolakha aftershock approaching, the strip-shaped MBT anomaly appeared again on May 11 and behaved most significantly on May 12, 2015 [also see Fig. 7(d)], corresponding to the adjustment and reaccumulation of the crustal stress at the junction of the Indian plate and the Eurasian–Asian plate. Subsequently, the MBT anomaly in the central study area dissipated with diminished seismicity.

Notably, some aftershocks of medium magnitude in the 2008 Wenchuan earthquake sequence, such as the Mw 5.6 aftershock on May 16 and the Mw 5.8 aftershock on May 17, 2008, corresponded well to the appearance of MBT anomaly along the LMSFs [see Fig. 7(a)], but the large aftershocks of the 2013 Lushan earthquake, such as the Mw 5.3 aftershock on April 24, 2013, did not show the same characteristics [see Fig. 7(c)]. Besides, some aftershocks of medium-to-large magnitude during the 2015 Nepal earthquake sequence, such as the Mw 6.7 aftershock on April 26 and the Mw 5.5 aftershock on May 16, 2015, exhibited no obvious MBT anomaly along the Himalayas, the time series of MBT anomaly around the epicenter only corresponded to the two major events [see Fig. 7(d)]. The inconsistent responses of MBT anomaly to the earthquake's magnitude were closely related to the specific changes of local stress state in each case. However, the dynamic variation of in-situ stress field and the geological environment are often unique and different, which brings some uncertainties to the revealed abnormal seismic MBT. Therefore, the study of different cases using multitemporal satellite observations should be combined with the actual situation.

E. Applications of the Results

As presented earlier, different data selection in frequency and polarization determines the morphology and intensity of MBT anomalies, whereas different earthquake case determines the location and temporal evolution of MBT anomalies. However, the inconsistency and uncertainty in results from different data and earthquake case can also provide a reference for routine research by comparing the characteristics of different results.

It is worth noting that, in addition to the difference in the degree of detail of the obtained results caused by the frequency difference, the more important feature is the different variation characteristics of the different anomalies with the frequency. For instance, as described in Fig. 2, the result of 2013 Lushan earthquake shows that the negative MBT anomaly west of the epicenter and the negative anomaly northeast of the epicenter on April 18 both become intense with the increase of frequency. But the result on April 19 shows that the positive MBT anomaly west of the epicenter becomes weak with the increase of frequency and even turns to be negative at 36.5 GHz. Through the comparative analysis of the results of two consecutive days, it is known that the two types of MBT anomalies on April 18 were most likely caused by clouds in the atmosphere or local meteorological effects, because of that the higher the frequency, the stronger the response shown to such disturbances. The results of daily surface soil moisture and quasi-synchronous atmospheric clouds in Fig. 8(a) and (b) demonstrate this inference that clouds passed over the area near the time of the microwave satellite image and soil moisture was at a low level. As for the results on April 19, the abnormal area west of the epicenter were most likely caused by disturbance from the ground because of that the higher the frequency, the weaker the response. Nor could this anomaly be due to the rise in soil moisture, since only high-frequency microwave channel (36.5 GHz) responded to it, and the low-frequency band (10.7 GHz), which is most sensitive to soil moisture, did not. It also indicates that the local meteorological effect of the previous day did not produce rainfall to increase the soil moisture west of the epicenter. Meanwhile, the negative anomaly east of the epicenter on April 19, according to this analytical method, was most likely to be related to changes in surface soil moisture. These assumptions are also confirmed by the results in Fig. 8(c) and (d) that soil moisture increased significantly in the labeled area while the study area was basically clear without clouds. Besides, this type of negative MBT anomaly of which the intensity decreased with the frequency also existed in the north side of the epicenter of the 2015 Nepal earthquakes, and the increasing of soil moisture in this area caused by quasi-synchronous precipitation was also confirmed in [45].

Note that polarization difference of MBT is often used in combination with microwave radiative transfer model to study vegetation change and retrieve soil moisture [46]. The polarization difference vertical minus horizontal (V–H) will increase as a result of the vegetation decrease [47]. Take the May 2008 Wenchuan earthquake as an example, the changes in polarization
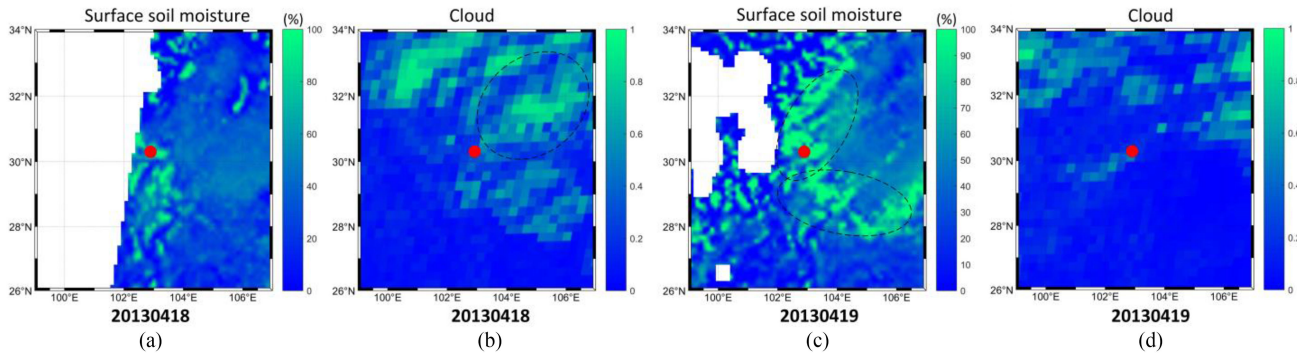
Fig. 8. Spatial distribution of soil moisture and cloud maps in the study area of Lushan earthquake on (a) April 18, 2013 and (b) April 19, 2013. Soil moisture is derived from AMSR2/GCOM-W1 daily surface soil moisture (LPRM) L3 dataset and cloud map is derived from FY-2D hourly cloud total amount dataset of which the imaging time is quasi-synchronous with that of used microwave images for 2013 Lushan earthquake.

difference vertical minus horizontal (V–H) show slight increasing along the LMSFs zone and in the southwest of the study area [see [48, Fig. 8]]. It was considered that the polarization difference in these areas might respond to the vegetation degradation. In practice, the study results of NDVI change before the May 2008 Wenchuan earthquake [49] were consistent with such speculation.

Therefore, by comparing and analyzing the multitemporal results with different frequencies and polarizations, some basic judgments can be made about the interference from atmospheric clouds, vegetation, rainfall, and soil moisture, and then, the interference of such nonseismic factors can be recognized first to retain potential seismic anomalies. The application of this analytical method will help to find more accurate information about earthquake-related anomalies from complex obtained results.

Furthermore, the results in Fig. 5 show inconsistency in spatial position and morphology of MBT anomalies of different earthquake cases. This suggests that due to the complexity process of earthquakes, MBT anomalies are difficult to be uniformly characterized. However, the relationship between MBT anomaly and tectonic environment can still be found through careful analysis. Qi *et al.* [48] reveal that two significant MBT positive anomalies of the May 2008 Wenchuan earthquake were exactly in spatial accordance with two geological Quaternary zones, and the detailed geometric information of the anomaly was correlated with the microwave frequencies. Qi *et al.* [45] show that the strip-shaped positive MBT anomaly of the 2015 Nepal earthquakes was parallel to the thrust belt and its intensity distributions exhibited good topographic consistency with the elevation profiles of the central Himalayas. The practical significance of these results lies in which it proves that seismogenic environment plays a decisive role in seismic MBT anomaly. When researchers try to monitor thermal anomaly in some specific areas, it is essential to pay more attention to local geological structure features and topographic features.

F. Limitation of the Approach and Analysis

In Section II, the establishment process of temporally weighted background based on multitemporal MBT images and the establishment process of spatially weighted background using these images in the study area are described in detail.

However, the effectiveness of interference information removal has always been an unavoidable problem. The temporally weighted background is to remove the inherent stable and general trend from satellite MBT observations, and random perturbations such as soil moisture or rainfall that exist in historical data will be smoothed out in the processing of long time nonseismic data. But these disturbances contained in the microwave images in the earthquake year will be involved in the calculation, because the contribution of these factors to MBT is difficult to be calculated quantitatively at present. The impurity pixels can only be determined and removed by auxiliary data. For instance, in Section IV-E, how to use multiband dual-polarization information to analyze the disturbance of factors such as soil moisture and vegetation has been discussed. The analysis and discussion are qualitative, which not only reflects the characteristics of the approach but also its limitations at present. In Figs. 2 and 3, the results of Lushan earthquake and Nepal earthquakes show obvious negative MBT residuals caused by soil moisture change, it adds to the complexity of the extraction. In the future, how to use the mapping relationship between multisource data, such as soil moisture, land surface temperature, land cover, and MBT, to quantitatively characterize the interference of soil moisture and other factors on MBT instead of directly removing the impurity pixels is worth further study.

The multifrequency characteristics of results indicated that the abnormal areas that become faint with the increasing of frequency could be identified as the anomalies that generated from the earth's surface, which are also the thermal anomalies most likely to be associated with earthquake activities. The limitation is that the determination of seismic MBT anomaly can only be made through the comparative analysis of multichannel data at present, which is still in the stage of manual interpretation. Although this can increase the reliability and geoscience rationality of obtained abnormal information, it also increases the complexity of the work at the same time. For instance, in [48], the impacts on MBT anomaly of May 2008 Wenchuan earthquake from surface temperature, vegetation index, land-surface roughness, and surface soil moisture have been discussed in terms of space, time, and magnitude, which requires extensive research results and complex analysis. If multiband dual-polarization data can be used to extract and determine the inherent characteristics of seismic MBT anomalies, then band

fusion, artificial intelligence big data, and other technologies will be introduced to automatically identify anomalies, which is of great significance to carry out numerous case studies all over the world.

It should also be noted that the method used in this article (STW-TSM) requires sufficient multitemporal MBT data to establish a temporally weighted background field, which will lead to a lack of data for studying the earthquakes that occurred in early years within the period covered by microwave satellite data. For instance, the temporal coverage of AMSR-E instrument was from June 2002 to October 2011, an earthquake that occurred at the end of 2002 could not be studied. In order to deal with the discontinuity of MBT data from single sensor in time and space, there have been many studies on the fusion method of satellite MBT data between different satellite platforms, which have not been but should have been applied in seismic anomaly research.

V. CONCLUSION AND OUTLOOK

Taking the May 2008 Wenchuan earthquake, the April 2010 Yushu earthquake, the April 2013 Lushan earthquake, and the 2015 Nepal earthquakes as four case studies, we analyzed and discussed the characteristics and uncertainties of seismic MBT anomaly. In the process of extracting seismic anomaly, different removal methods of historical background field lead to obvious uncertainties in the obtained results. The revealed multitemporal seismic anomalies suggested that the spatiotemporally dynamic description of influencing factors was more beneficial in restraining the inherent disturbances embedded in satellite MBT. Moreover, the revealed time series of MBT anomalies associated with the four earthquake cases showed significant inconsistencies using different frequencies and polarizations of MBT data, and the abnormal amplitude and spatiotemporal pattern of MBT anomalies were closely related to the selection and process of satellite MBT data. MBT data with 10.7 GHz at H polarization were recommended as a more efficient microwave band for seismic thermal anomaly monitoring. Meanwhile, the spatiotemporal evolutions of MBT anomaly and time series of average MBT anomaly before, during, and after the 2008 Wenchuan earthquake, the 2010 Yushu earthquake, the 2013 Lushan earthquake, and the 2015 Nepal earthquakes were analyzed, and the emergences and evolutions of MBT anomaly were found to be closely related to the seismogenic process and the structures of control faults. Thus, inherent relations between seismic anomalies and seismogenic mechanisms were implied, and uncertainties in the results of different earthquake cases were exhibited. Furthermore, the applications of multifrequency and dual polarization data were introduced and the limitations of the approach as well as the analytical method were discussed.

In this research, the comprehensive comparison and analysis of seismic MBT anomaly on the basis of different methods used, data used, and case studies are instructive for remote sensing data selection and abnormal phenomenon interpretation, although there are some shortcomings due to the complexity of the revealed results. It is suggested from the analysis that MBT data with lower frequencies is more desirable for detecting thermal anomaly related to some large earthquakes with broader seismogenic preparation zone, whereas MBT data with higher frequencies maybe more suitable for retrieving slight thermal anomaly associated with some small-to-medium earthquakes on the premise of effectively nonseismic noise removing or restraining. This study also embodied that summarizing the characteristics of earthquake anomaly and analyzing the uncertainties in abnormal phenomena, from a multitemporal perspective, are conducive to exploring actual causes of seismic anomaly. Furthermore, numerous case studies help to explore the regularity and draw general conclusion, so that statistics and analysis of uncertainties in seismic anomaly using artificial intelligence big data are worthy of trying.

REFERENCES

[1] V. Gorny, A. Salman, A. Tronin, and B. Shilin, "Terrestrial outgoing infrared radiation as an indicator of seismic activity," *Proc. Acad. Sci. USSR*, vol. 301, pp. 67–69, 1988.

[2] A. A. Tronin, "Satellite thermal survey—A new tool for the study of seismoactive regions," *Int. J. Remote Sens.*, vol. 17, pp. 1439–1455, 1996.

[3] A. A. Tronin, M. Hayakawa, and O. A. Molchanov, "Thermal IR satellite data application for earthquake research in Japan and China," *J. Geodyn.*, vol. 33, no. 3/4, pp. 519–534, 2002.

[4] X. D. Xu, Z. J. Qiang, and C. G. Dian, "Thermal anomaly and temperature increase before impending earthquake," *Chin. Sci. Bull.*, vol. 6, pp. 291–294, 1991.

[5] A. K. Saraf and S. Choudhury, "Satellite detects surface thermal anomalies associated with the Algerian earthquakes of May 2003," *Int. J. Remote Sens.*, vol. 26, no. 13, pp. 2705–2713, 2004.

[6] A. K. Saraf and C. Swapnamita, "Thermal remote sensing technique in the study of pre-earthquake thermal anomalies," *J. Ind. Geophys.*, vol. 9, no. 3, pp. 197–207, 2005.

[7] V. Tramutoli, V. Cuomob, C. Filizzola, N. Pergola, and C. Pietrapertosa, "Assessing the potential of thermal infrared satellite surveys for monitoring seismically active areas: The case of Kocaeli (Izmit) earthquake," *Remote Sens. Environ.*, vol. 96, no. 3/4, pp. 409–426, 2005.

[8] D. Ouzounov, N. Bryant, T. Logan, S. Pulinets, and P. Taylor, "Satellite thermal IR phenomena associated with some of the major earthquakes in 1999–2003," *Phys. Chem. Earth Parts A/B/C*, vol. 31, no. 4–9, pp. 154–163, 2006.

[9] L. X. Wu, K. Qin, and S. J. Liu, "GEOSS-based thermal parameters analysis for earthquake anomaly recognition," *Proc. IEEE*, vol. 100, no. 10, pp. 2891–2907, Oct. 2012.

[10] K. Qin, L. X. Wu, and W. Ma, "Discriminating satellite IR anomalies associated with the MS 7.1 Yushu earthquake in China," *Adv. Space Res.*, vol. 61, no. 5, pp. 1324–1331, 2018.

[11] Y. Zhang and Q. Meng, "A statistical analysis of TIR anomalies extracted by RSTs in relation to an earthquake in the Sichuan area using MODIS LST data," *Natural Hazard Earth Syst. Sci.*, vol. 19, no. 3, pp. 535–554, 2019.

[12] N. Ahmad *et al.*, "Investigation of spatio-temporal satellite thermal IR anomalies associated with the Awaran earthquake (Sep 24, 2013; M 7.7), Pakistan," *Pure Appl. Geophys.*, vol. 176, no. 8, pp. 3533–3544, 2019.

[13] D. Ouzounov and F. Freund, "Mid-infrared emission prior to strong earthquakes analyzed by remote sensing data," *Adv. Space Res.*, vol. 33, no. 3, pp. 268–273, 2004.

[14] T. Maeda and T. Takano, "Discrimination of local and faint changes from satellite-borne microwave-radiometer data," *IEEE Trans. Geosci. Remote Sens.*, vol. 46, no. 9, pp. 2684–2691, Sep. 2008.

[15] T. Maeda and T. Takano, "Detection of microwave signals associated with rock failures in an earthquake from satellite-borne microwave radiometer data," in *Proc. Int. Geosci. Remote Sens. Symp.*, 2009, pp. 61–64.

[16] T. Maeda and T. Takano, "Detection algorithm of earthquake-related rock failures from satellite-borne microwave radiometer data," *IEEE Trans. Geosci. Remote Sens.*, vol. 48, no. 4, pp. 1768–1776, Apr. 2010.

[17] H. Chen and Y. Q. Jin, "A preliminary detection of anomalous radiation of rock failures related with Yushu earthquake by using satellite-borne microwave radiometers," *Remote Sens. Technol. Appl.*, vol. 25, no. 6, pp. 860–866, 2011.

[18] R. P. Singh *et al.*, "Precursory signals using satellite and ground data associated with the Wenchuan earthquake of 12 May 2008," *Int. J. Remote Sens.*, vol. 31, no. 13, pp. 3341–3354, 2010.

[19] F. Jing, R. P. Singh, K. Sun, and X. H. Shen, "Passive microwave response associated with two main earthquakes in Tibetan Plateau, China," *Adv. Space Res.*, vol. 62, no. 7, pp. 1675–1689, 2018.

[20] F. Jing, R. P. Singh, and X. Shen, "Land–atmosphere–meteorological coupling associated with the 2015 Gorkha (M 7.8) and Dolakha (M 7.3) Nepal earthquakes," *Geomatics, Natural Hazards, Risk*, vol. 10, no. 1, pp. 1267–1284, 2019.

[21] J. Yang and G. M. Guo, "Preliminary analysis of thermal anomalies before the 2010 Baja California M7.2 earthquake," *Atmosfera*, vol. 26, no. 4, pp. 473–477, 2013.

[22] Y. Qi, L. Wu, M. He, and W. Mao, "Spatio-temporally weighted two-step method for retrieving seismic MBT anomaly: May 2008 Wenchuan earthquake sequence being a case," *IEEE J. Sel. Topics Appl. Earth Observ. Remote Sens.*, vol. 13, pp. 382–391, May 2020.

[23] F. Jing, R. P. Singh, Y. Cui, and K. Sun, "Microwave brightness temperature characteristics of three strong earthquakes in Sichuan Province, China," *IEEE J. Sel. Topics Appl. Earth Observ. Remote Sens.*, vol. 13, pp. 513–522, Jan. 2020.

[24] F. T. Ulaby, R. K. Moore, and A. K. Fung, *Microwave Remote Sensing: Active and Passive. Volume 1—Microwave Remote Sensing Fundamentals and Radiometry*. Boston, MA, USA: Addison-Wesley, 1981, pp. 181–224.

[25] W. Ma, W. Ma, H. Zhao, and H. Li, "Temperature changing process of the Hokkaido (Japan) earthquake on 25 September 2003," *Natural Hazards Earth Syst. Sci.*, vol. 8, pp. 985–989, 2008.

[26] K. Qin, L. X. Wu, S. Zheng, and S. J. Liu, "A deviation-time-space-thermal (DTS-T) method for global earth observation system of systems (GEOSS)-based earthquake anomaly recognition: Criterions and quantify indices," *Remote Sens.*, vol. 5, no. 10, pp. 5143–5151, 2013.

[27] X. Z. Yang *et al.*, "The hypocenter and origin time of the Mw 7.9 Wenchuan earthquake of May 12, 2008," *Acta Seismol. Sin.*, vol. 32, no. 2, pp. 127–136, 2012.

[28] X. Xu *et al.*, "Coseismic reverse- and oblique-slip surface faulting generated by the 2008 Mw 7.9 Wenchuan earthquake, China," *Geology*, vol. 37, no. 6, pp. 515–518, Jun. 2009.

[29] Y. T. Chen, Z. X. Yang, and Y. Zhang, "From 2008 Wenchuan earthquake to 2013 Lushan earthquake (in Chinese)," *Scientia Sin. Terrae*, vol. 43, no. 6, pp. 1064–1072, 2013.

[30] B. Shan *et al.*, "Stress changes on major faults caused by 2013 Lushan earthquake, and its relationship with 2008 Wenchuan earthquake," *Sci. China: Earth Sci.*, vol. 43, no. 6, pp. 1002–1009, 2013.

[31] F. Du *et al.*, "The M7.0 Lushan earthquake and the relationship with the M8.0 Wenchuan earthquake in Sichuan, China," *Chin. J. Geophys. (Chin.)*, vol. 56, no. 5, pp. 1772–1783, 2013.

[32] L. Chen *et al.*, "The Ms 7.1 Yushu earthquake surface rupture and large historical earthquakes on the Garzê-Yushu fault," *Chin. Sci. Bull.*, vol. 55, no. 31, pp. 3504–3509, 2010.

[33] G. M. Zhao, J. Liu, and Z. H. Wu, "The 2015 Nepal earthquake and the future trend of the Himalayan orogen," *J. Geomech.*, vol. 21, no. 3, pp. 351–358, 2015.

[34] T. Kawanishi *et al.*, "The advanced microwave scanning radiometer for the earth observing system (AMSR-E), NASDA's contribution to the EOS for global energy and water cycle studies," *IEEE Trans. Geosci. Remote Sens.*, vol. 41, no. 2, pp. 184–194, Feb. 2003.

[35] X. L. Zou, J. Zhao, F. Z. Weng, and Z. K. Qin, "Detection of radio-frequency interference signal over land from FY-3B microwave radiation imager (MWRI)," *IEEE Trans. Geosci. Remote Sens.*, vol. 50, no. 12, pp. 4994–5003, Dec. 2012.

[36] M. Zoran, "MODIS and NOAA-AVHRR l and surface temperature data detect a thermal anomaly preceding the 11 March 2011 Tohoku earthquake," *Int. J. Remote Sens.*, vol. 33, pp. 6805–6817, 2012.

[37] L. X. Wu *et al.*, "Geosphere coupling and hydrothermal anomalies before the 2009 Mw 6.3 L'Aquila earthquake in Italy," *Natural Hazards Earth Syst. Sci.*, vol. 16, no. 8, pp. 1859–1880, 2016.

[38] W. Y. Ma *et al.*, "Influences of multiple layers of air temperature differences on tidal forces and tectonic stress before, during and after the Jiujiang earthquake," *Remote Sens. Environ.*, vol. 210, pp. 159–165, 2018.

[39] J. Xiao, "Dielectric properties of minerals and rocks and their application in remote sensing," *Remote Sens. Environ. (Chin.)*, vol. 3, no. 2, pp. 135–146, 1988.

[40] Y. H. Kerr and E. G. Njoku, "A semiempirical model for interpreting microwave emission from semiarid land surfaces as seen from space," *IEEE Trans. Geosci. Remote Sens.*, vol. 28, no. 3, pp. 384–393, May 1990.

[41] X. Xu, *Album of 5.12 Wenchuan 8.0 Earthquake Surface Ruptures*. Beijing, China: Seismol. Press, 2009.

[42] W. L. Wang, J. P. Wu, L. H. Fang, and C. Wang, "Relocation of the Yushu Ms7.1 earthquake and its aftershocks in 2010 from HypoDD," *Sci. China: Earth Sci.*, vol. 42, no. 7, pp. 1037–1046, 2012.

[43] S. Xin-Zhe *et al.*, "Surface rupture features of the 2010 Yushu earthquake and its tectonic implication," *Chin. J. Geophys. (Chin.)*, vol. 55, no. 1, pp. 155–170, 2012.

[44] G. P. Hayes and R. W. Briggs, "Introduction to the special issue on the 25 April 2015 Mw 7.8 Gorkha (Nepal) earthquake," *Tectonophysics*, vol. 714, pp. 1–3, 2017.

[45] Y. Qi, L. X. Wu, Y. F. Ding, and W. F. Mao, "Microwave brightness temperature anomalies associated with the 2015 Mw 7.8 Gorkha and Mw 7.3 Dolakha earthquakes in Nepal," *IEEE Trans. Geosci. Remote Sens.*, 2020.

[46] M. Owe, J. Richard, and J. Walker, "A methodology for surface soil moisture and vegetation optical depth retrieval using the microwave polarization difference index," *IEEE Trans. Geosci. Remote Sens.*, vol. 39, no. 8, pp. 1643–1654, Aug. 2001.

[47] C. Prigent, F. Aires, and W. B. Rossow, "Land surface microwave emissivities over the globe for a decade," *Bull. Amer. Meteorol. Soc.*, vol. 87, no. 11, pp. 1573–1584, 2006.

[48] Y. Qi, L. Wu, W. Mao, Y. Ding, and M. He, "Discriminating possible causes of microwave brightness temperature positive anomalies related with May 2008 Wenchuan earthquake sequence," *IEEE Trans. Geosci. Remote Sens.*, vol. 59, no. 3, pp. 1903–1916, Mar. 2021.

[49] B. Ma, L. Wu, and S. Liu, "NDVI variation features before Wenchuan Ms 8.0 earthquake," *Sci. Technol. Rev.*, vol. 28, no. 13, pp. 52–57, 2010.

Yuan Qi (Graduate Student Member, IEEE) received the B.S. degree in surveying and mapping engineering from Northeastern University, Shenyang, China, in 2017. He is currently working toward the Ph.D. degree in photogrammetry and remote sensing with Central South University, Changsha, China.

His research interests include seismic thermal anomaly monitoring, geohazard perception and cognition, and remote sensing rock mechanics.

Zelang Miao (Member, IEEE) received the B.S. degree in surveying engineering and the M.S. degree in geodesy and surveying engineering from the China University of Mining and Technology, Xuzhou, China, in 2009 and 2014, respectively, and the Ph.D. degree in satellite image processing from The Hong Kong Polytechnic University, Hong Kong, in 2016.

He was a visiting Ph.D. Student with the Department of Industrial and Information Engineering, University of Pavia, Pavia, Italy, in 2015. He is currently an Associate Professor with the School of Geoscience and Info-Physics, Central South University, Changsha, China. He has authored or coauthored more than 30 papers on international and peer-reviewed scientific journals. His research interests include pattern recognition, land cover, land-use mapping, and global/regional urbanization.

Dr. Miao is a referee for the IEEE TRANSACTIONS ON GEOSCIENCE AND REMOTE SENSING and the IEEE JOURNAL OF SELECTED TOPICS IN APPLIED EARTH OBSERVATION AND REMOTE SENSING.

Lixin Wu received the B.S. degree in mining survey from the China University of Mining and Technology, Xuzhou, China, in 1988, and the M.S. and Ph.D. degrees in geomatics from the China University of Mining and Technology (Beijing), Beijing, China, in 1991 and 1997, respectively.

He is currently with Central South University, Changsha, China, as a leading Professor of Geomatics with the School of Geoscience and Info-Physics.

Dr. Wu was a former Co-Chair of User Applications in Remote Sensing Committee, IEEE Geoscience, and Remote Sensing Society. He is currently a member of the Global Risk Assessment Framework Expert Group of the United Nations, a member of the Infrastructure Implementation Board of Group on Earth Observation, the Chairman of WG III-8 of International Society for Photogrammetry and Remote Sensing, a member of the China National Committee of the International Society for Digital Earth, the Vice-Chairman of the Space Observation Committee of the China Seismology Society, and the Editor-in-Chief of the *Journal of Geography and Geo-Information Science* (Chinese).

Yifan Ding received the B.S. degree in surveying and mapping engineering in 2019 from Central South University, Changsha, China, where he is currently working toward the M.S. degree in photogrammetry and remote sensing.

His research interest includes seismic thermal anomaly monitoring.